



This is a repository copy of *Correlating nanoscale morphology with device performance in conventional and inverted PffBT4T-2OD:PC71BM polymer solar cells*.

White Rose Research Online URL for this paper:
<http://eprints.whiterose.ac.uk/156039/>

Version: Accepted Version

Article:

Yan, Y., Li, W., Cai, F. et al. (7 more authors) (2018) Correlating nanoscale morphology with device performance in conventional and inverted PffBT4T-2OD:PC71BM polymer solar cells. *ACS Applied Energy Materials*, 1 (7). pp. 3505-3512. ISSN 2574-0962

<https://doi.org/10.1021/acsaem.8b00727>

This document is the Accepted Manuscript version of a Published Work that appeared in final form in *ACS Applied Energy Materials*, copyright © American Chemical Society after peer review and technical editing by the publisher. To access the final edited and published work see <https://doi.org/10.1021/acsaem.8b00727>

Reuse

Items deposited in White Rose Research Online are protected by copyright, with all rights reserved unless indicated otherwise. They may be downloaded and/or printed for private study, or other acts as permitted by national copyright laws. The publisher or other rights holders may allow further reproduction and re-use of the full text version. This is indicated by the licence information on the White Rose Research Online record for the item.

Takedown

If you consider content in White Rose Research Online to be in breach of UK law, please notify us by emailing eprints@whiterose.ac.uk including the URL of the record and the reason for the withdrawal request.



eprints@whiterose.ac.uk
<https://eprints.whiterose.ac.uk/>

Correlating Nanoscale Morphology with Device Performance in Conventional and Inverted PffBT4T-2OD:PC₇₁BM Polymer Solar Cells

Yu Yan¹, Wei Li¹, Feilong Cai¹, Jinlong Cai¹, Zhiwei Huang¹, Robert S. Gurney¹, Dan Liu¹, David G. Lidzey², Andrew J. Pearson³, Tao Wang^{1}*

1 School of Materials Science and Engineering, Wuhan University of Technology, Wuhan, 430070, China E-Mail: twang@whut.edu.cn

2 Department of Physics and Astronomy, University of Sheffield, Sheffield, S3 7RH, UK

3 Cavendish Laboratory, University of Cambridge, JJ Thomson Avenue, Cambridge, CB3 0HE, UK

KEYWORDS: Polymer solar cell, organic photovoltaics, nanoscale morphology, vertical component distribution, device efficiency, PffBT4T-2OD

ABSTRACT: Nanoscale morphology has been established as one of the controlling factors in the device performance of bulk heterojunction polymer solar cells. We report in this work morphology changes in both lateral and vertical directions in PffBT4T-2OD:PC₇₁BM solar cells, as well as their effects on device performance. Thermal annealing was found to increase the crystallinity of PffBT4T-2OD and domain size of PC₇₁BM clusters without any observable impact on vertical component redistribution, whilst methanol rinsing reduces the crystallinity of PffBT4T-2OD, encourages the migration of PC₇₁BM towards the mixed polymer-rich phase as well as towards the film surface on both PEDOT:PSS and TiO₂ substrates. The polymer-rich surface region in vacuum- and thermal annealing- treated conventional devices obstructs electron injection towards the cathode, and reduces the maximum achievable device efficiency, whilst this polymer-rich surface region is beneficial in the

inverted devices. However, although a PC₇₁BM-rich region will locate at the cathode or anode interface upon methanol rinsing treatment in conventional and inverted devices respectively, holes can still be effectively injected from both sides the device to ensure effective charge transport, as supported by a number of optoelectronic property investigations.

1. INTRODUCTION

Polymer solar cells (PSCs), especially with bulk heterojunction (BHJ) structure, benefit from their low material costs and advantages of solution-processing, and have been regarded as a promising candidate for the next generation renewable energy sources.¹⁻³ BHJ-based devices, which consist of multiple length-scale phase-separated electron donors and acceptors, facilitate charge separation at the donor/acceptor interface and charge transport through an interpenetrating network. Over the past decade, tremendous efforts from molecular tailoring, morphology control and interfacial engineering have greatly boosted the power conversion efficiency (PCE) of laboratory scaled PSCs to over 14%.⁴⁻⁵

However, due to the relatively low charge mobilities in organic semiconductors, most PSCs have an optimized film thickness around 100 nm to balance the photo-absorption and charge transport, which may otherwise seriously restrict the practical transition of those high performing PSCs to industrial fabrication.⁶⁻⁸ To meet mass production requirements, PSCs with thick photoactive layers without compromised performance are desired. To this end, a series of high-mobility conjugated polymers based on the difluorobenzothiadiazole or naphthobisthiadiazole building blocks have been developed, which exhibited a highest PCE of over 10% with the thickness of the BHJ layer over ~250 nm, with poly[(5,6-difluoro-2,1,3-benzothiadiazol-4,7-diyl)-alt-(3,3''-di(2-octyldodecyl)-2,2';5',2'';5'',2'''-quarterthiophen-5,5'''-diyl)] (PffBT4T-2OD) as one promising electron-donating polymer from this family.⁹⁻¹⁰ PffBT4T-2OD has been found to display temperature-dependent aggregation behavior, and can form desired morphology that contains highly crystalline yet reasonably small polymer domains. Although relatively good devices nearing 11% can be achieved in

PffBT4T-2OD:PC₇₁BM solar cells, this photovoltaic device has been found to be unstable and degrades at a fairly fast rate due to decomposition within the solid photovoltaic film.¹¹ This decomposition originates from its thermal-dynamic instability, and is exacerbated with the presence of a high boiling point solvent additive such as 1,8-diiodooctane (DIO), which is added to the solution to promote the formation of ideal morphology but partly remains due to its slow evaporation rate during the film casting process.^{12,13}

In this work, we have applied three solvent extraction methods, herein referred as vacuum extraction (VA), thermal-annealing extraction (TA) and methanol-rinsing extraction (MA), to remove the residual DIO which can contribute to enhance the device efficiency and stability. We found that these three post-treatments result in different nanoscale morphologies, notably with methanol rinsing reducing the crystallinity of the PffBT4T-2OD phase and promoting the migration of PC₇₁BM towards the film surface that was originally polymer-rich in the as-cast film. The impacts of these vertical component distributions, however, depend on the device configurations (i.e. direct and inverted device structures).

2. EXPERIMENTAL SECTION

TiO₂ nanoparticles were synthesized following our previous report,¹⁴ with as-synthesized TiO₂ precipitated and purified three times with diethylether before further use. The precipitate was collected and dispersed in 2-methoxyethanol by ultrasonication to prepare a TiO₂ dispersion with a solid content of ~5 mg/mL. To modify the TiO₂ dispersion, 30 μ L of titanium(diisopropoxide) bis(2,4-pentanedioate) (TIPD) was added into 2 mL of the TiO₂ dispersion, and agitated for 2 h to allow efficient blending. The dispersions were stored in a refrigerator at least 48 h before use. TIPD will convert to titanium oxide bis(2,4-pentanedionate) (TOPD) after losing the isopropoxide group upon thermal annealing, to reduce the porosity and surface roughness of TiO₂ films, and enable an efficient TiO₂:TOPD electron transport layer (ETL).

Inverted PSCs are constructed with the structure of ITO/TiO₂:TOPD (20 nm)/PffBT4T-2OD:PC₇₁BM (250 nm)/MoO₃ (10 nm)/Ag (100 nm). Pre-patterned ITO-glass substrates with sheet resistance $\approx 15 \text{ } \Omega/\text{sq}$ were cleaned by ultrasonication sequentially in water, acetone, ethanol, and isopropyl alcohol each for 10 min and then dried at 140 °C on a hotplate. Cleaned ITO substrates were further treated with UV-O₃ for 10 min. The TiO₂:TOPD ETL was cast from the TiO₂:TIPD dispersion at 3000 rpm, followed by thermal annealing at 155 °C for 30 min to create a $\approx 20 \text{ nm}$ thick thin film. All processes were performed in an ambient environment. Then the coated TiO₂:TOPD ETL substrates were transferred to an N₂-filled glovebox to cast the active layer. PffBT4T-2OD:PC₇₁BM blends (w/w, 1:1.2) were prepared in a CB/DCB mixture (v/v, 1:1) with 3% of DIO (polymer concentration: 9 mg mL⁻¹). To completely dissolve the polymer, the active layer solution was stirred on a hot plate at 110 °C for at least 3 h. The ITO substrates were also preheated on a hot plate at $\sim 110 \text{ } ^\circ\text{C}$ before spin-coating. Then the preheated ITO substrates were transferred to the spin coater chuck and casting of films was completed within 10 s. The wet films were spun at 800 rpm for 40 s, and then at 4000 rpm for 20 s to create a film of $\sim 250 \text{ nm}$. For the vacuum-treated (VA) samples, the as-cast films were immediately sent to the vacuum chamber and kept overnight ($\sim 12 \text{ h}$) under a high vacuum ($\sim 10^{-7} \text{ torr}$) to completely remove the residual DIO. For thermally annealed (TA) samples, the as-cast films were heated on a hot plate at 100 °C for 5 min, which lies between the glass transition temperature (T_g , *ca.* 90 °C) and the melting temperature (T_m , *ca.* 260 °C) of PffBT4T-2OD to modify the crystallinity and phase separation in the blend.^{11,15,16} For methanol rinsed (MA) samples, the as-cast films were rinsed with 200 μl methanol at 4000 rpm for 20 s. Finally, 10 nm MoO₃ and 100 nm Ag were deposited onto the photoactive layer through shadow masks by thermal evaporation, defining the size of each active area as 4 mm².

For the direct configuration devices, 40 nm PEDOT:PSS (Clevios, AI 4083, Heraeus, Germany) films were cast on the pre-cleaned ITO substrates as the hole transport layer. The films were then

dried at 135 °C for 20 min before depositing the photoactive layer following the same procedure as described above. Finally 5 nm Ca and 100 nm Ag were thermally evaporated forming a cathode under high vacuum. All the devices were encapsulated with UV-curable epoxy glue and glass slides before removing from the glovebox for device testing.

Current density-voltage (J-V) curves under AM 1.5G illumination (100 mW/cm²) were measured with programmable J-V sweep software developed by Ossila Ltd. (Sheffield, UK). Before J-V testing, the intensity of the Newport 3A solar simulator was first calibrated with a NREL-certified silicon reference cell. An aperture mask was placed over the devices to accurately define a test area of 2.12 mm² on each pixel and to eliminate the influence of stray and wave-guided light. Surface morphology of the active layer was characterized by atomic force microscopy (AFM, NT-MDT, Russia). Transmission electron microscopy (TEM, JEOL, Japan) was also performed for a plan-view of the bulk morphology of the active layer. PffBT4T-2OD:PC₇₁BM films were floated off the substrates by dissolving the water-soluble PEDOT:PSS in DI-water and then lifted by the copper grids for TEM characterization. Water contact angle measurements were performed using a water contact angle measurement system (Attension Theta Lite, Sweden), and the surface energy was calculated using the equation of state. The absorption of the films were measured with a UV-Vis Spectrophotometer (HITACHI, Japan) equipped with the integrating sphere. Film thickness measurements were conducted using a spectroscopic ellipsometer (J. A. Woollam, USA). Synchrotron grazing incidence small-angle X-ray scattering (GISAXS) measurements were conducted using the beamline BL16B1 at the Shanghai Synchrotron Radiation Facility (SSRF) in China. Grazing incidence wide-angle X-ray scattering (GIWAXS) measurements were conducted using the beamline I07 at Diamond Light Source in the U.K. The energy of the X-ray beam was 10 keV and the incident angle varied from 0.12 to 0.25°. Samples were prepared on Si substrates and received the same processing procedure as used

in devices. XPS measurements were conducted by using a Thermo Fisher Scientific PHI Quantera II system with a monochromatic Al K α source.

3. RESULTS AND DISCUSSION

The PC₇₁BM-selective solvent DIO was added to tune the aggregation size of the electron acceptor PC₇₁BM in order to improve the efficiency of PSCs.¹⁰ However, due to its high boiling point, DIO has also been found to remain in the active layer of the device, where its presence acts as charge traps that deteriorate device performance and lifetime.¹² We therefore have applied three DIO extraction methods: VA, TA and MA to remove DIO from the as-cast films. As TA- and MA- treated films will inevitably receive further vacuum treatment during the cathode or anode deposition process, VA- treated films essentially serve as the reference here to examine the effects of TA and MA. Since charge generation and recombination behaviors are closely related to the nanoscale morphology in both lateral and vertical directions,^{17,18} a number of surface and bulk characterizations have been performed to obtain these data. First of all, it is obvious that the crystalline fibrils can be observed in the bulk of all samples under transmission electron microscopy (TEM) due to the strong temperature-dependent aggregation behavior of PffBT4T-2OD during the film casting process,^{9,19} with slightly enhanced crystallinity in the TA-treated blend film (Figure 1a-c). These variations in the bulk of the film were confirmed by the surface morphology observed with atomic force microscopy. As shown in Fig. 1d-f, more fibril features can be observed in the TA-treated film surface, with an associated enhancement of surface roughness due to the increased crystallinity of PffBT4T-2OD. The MA-treated blend, however, displayed reduced fibril-like features and a smoother surface via AFM characterization, indicating reduced crystallinity of PffBT4T-2OD and surface coverage by the migration of fullerene.

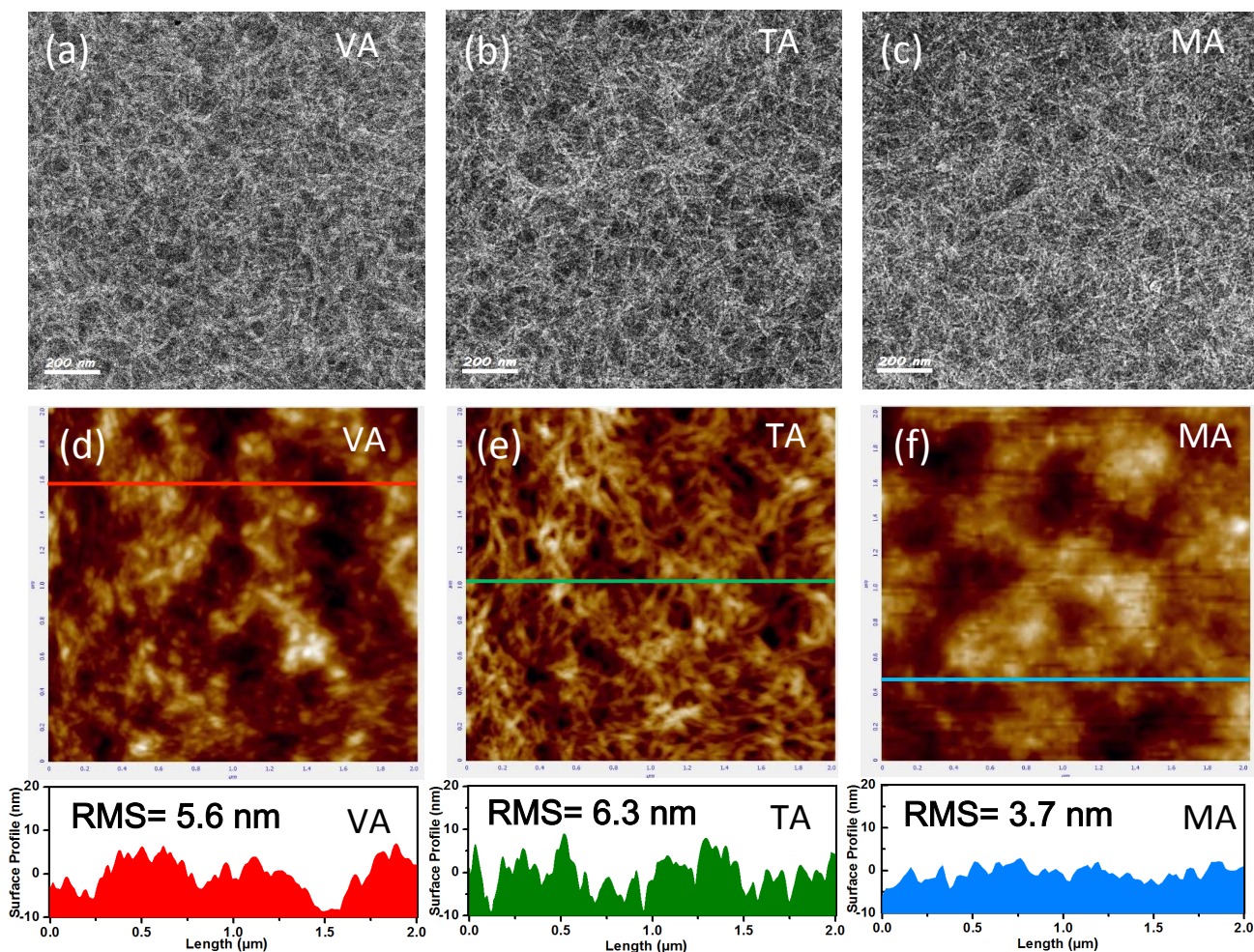


Figure 1. TEM (top) plan-view and AFM (bottom) surface images of PffBT4T-2OD:PC₇₁BM films upon (a and d) VA, (b and e) TA, (c and f) MA post-treatment. Below the AFM images the corresponding Root-Mean-Square (RMS) surface roughnesses are shown. AFM images are 2 x 2 μm².

GIWAXS and GISAXS characterizations using synchrotron X-ray sources have also been performed to confirm the variations of the PffBT4T-2OD crystallinity upon these three different post-treatments, and provide information on the domain sizes of the polymer and fullerene phases, which TEM and AFM cannot measure precisely due to limits in spatial resolution and phase contrast. The 1D profiles of the 2D GIWAXS patterns show the (100) lamella and (010) π - π stacking diffraction peaks of PffBT4T-2OD at 0.3 and 1.76 Å⁻¹ respectively, suggesting that thermal annealing and methanol rinsing treatments increased and reduced the diffraction intensity of lamella crystalline and π - π stacking of PffBT4T-2OD. A similar conclusion can be drawn on the aggregation of PC₇₁BM

based on its diffraction peak at $\sim 1.34 \text{ \AA}^{-1}$. GIWAXS measurements therefore support the previous findings by TEM and AFM measurements. GISAXS patterns of three post-treated PffBT4T-2OD:PC₇₁BM film on the same type of substrates are shown in Figure 2e, and the 1D in-plane GISAXS profiles are extracted and shown in Figure 2f and then fitted with a combination of the Debye-Anderson-Brumberger equation (DAB model) and Fractal model using software SasView.

The best fitting parameters are summarized in Table 1. In the 1D GISAXS profiles, enhanced scattering intensities in the low-Q region are mainly attributed to the PC₇₁BM-dispersed polymer-rich phase, and can be characterized by the correlation length ζ in the DAB model.²⁰ In Table 1, the correlation length ζ of VA-treated material is around 26 nm, which is close to the reported value of around 30 nm obtained by resonant soft X-ray scattering.⁹ This relatively long correlation length can be ascribed to the fast quenching process after film casting using a hot solution that leaves more open structure within the photovoltaic film. After TA treatment, this correlation length ζ reduced to 20 nm, partly as a result of the reduced open space upon thermal annealing. Another origin can be attributed to the diffusion of PC₇₁BM particles out of the polymer-rich phases, which will reduce the correlation length of the polymer-rich phase but increase the correlation length of PC₇₁BM cluster domain from 35.1 to 39.5 nm. This correlation length of the PC₇₁BM cluster domain is represented by $2R_g$ (where R_g is the Guinier radius) and is a product of parameters η and D , which are the correlation length and fractal dimension of the fractal-like network of PC₇₁BM.^{21,22} Remarkably, we found opposite changes after MA treatment, that the correlation length of the polymer-rich phase increased to 41.6 nm and the size of the PC₇₁BM cluster domain reduced to 33.8 nm, which suggests that the PC₇₁BM particles started to dissociate from their close-packed clusters and diffused into the polymer-rich phase during methanol rinsing. Our GIWAXS measurements already confirmed that the crystallinity of PffBT4T-2OD decreased upon MA treatment, that is to say, the number of less-ordered and amorphous regions increased. After film casting, the residual DIO with extremely low volatility will primarily distribute

among PC₇₁BM particles due to a better miscibility between the two materials. The low-boiling-point methanol has high volatility and good miscibility with DIO, which can rapidly drive DIO molecules and PC₇₁BM particles vertically towards film surface (results will be discussed further in the following section) during MA treatment, an effect that will lead to the redistribution of PC₇₁BM into the polymer-rich phase to reduce the polymer crystallinity.

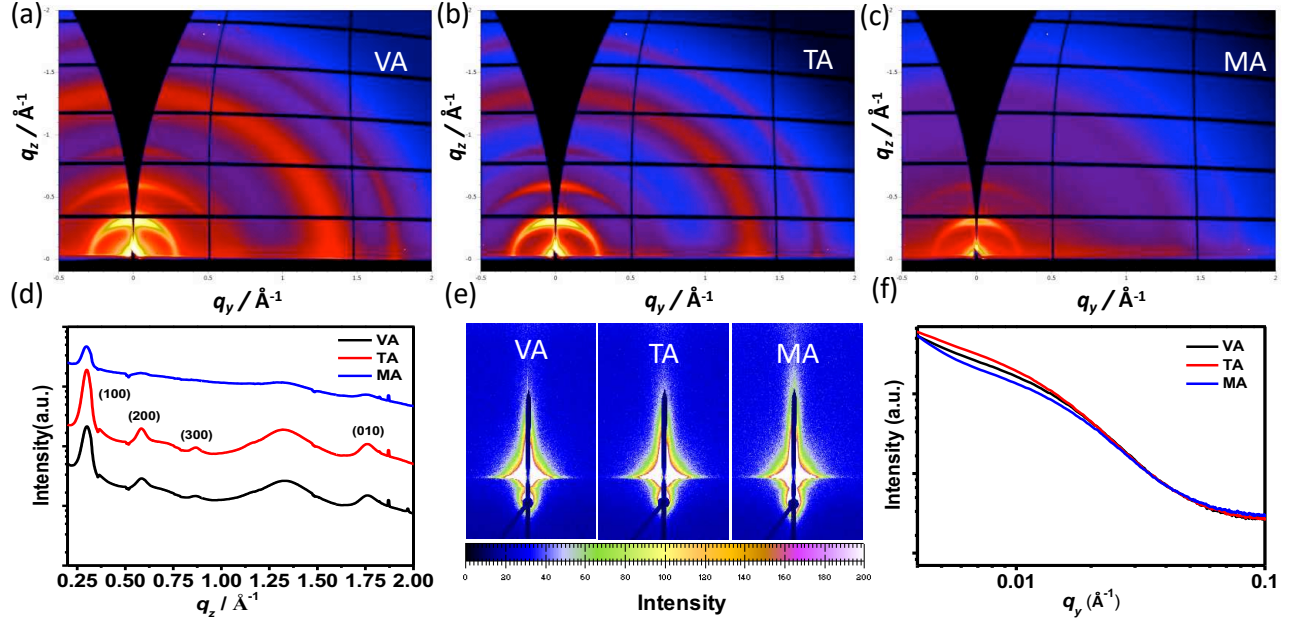


Figure 2. 2D GIWAXS patterns of PffBT4T-2OD:PC₇₁BM film upon (a) VA, (b) TA and (c) MA treatments, and (d) the corresponding 1D profiles in the q_z (out-of-plane) direction. (e) 2D GISAXS patterns and (f) the corresponding 1D profiles along the q_y (in-plane) direction.

Table 1. Fitting parameters of 1D GISAXS profiles of PffBT4T-2OD:PC₇₁BM films with different DIO extraction procedures

Procedure	ζ [nm]	η [nm]	D	$2R_g$ [nm]
VA	26.0	7.3	2.94	35.1
TA	20.0	8.2	2.94	39.5
MA	41.6	7.1	2.90	33.8

ζ represents the average correlation length of the fullerene-dispersed polymer phase, which can be fitted in the low- Q region with the DAB model. η and D are the correlation length of PCBM aggregation and fractal dimensionality of PCBM cluster extracted from the Fractal model, respectively. R_g represented the Guinier radius (R_g) of the clustered fullerene phase, calculated with

$$R_g = \sqrt{\left(\frac{D(D+1)}{2}\right)} \eta.$$

To complete the three-dimensional nanoscale morphology changes of PffBT4T-2OD:PC₇₁BM upon these three types of post-treatments, we have further investigated the component distributions in the vertical direction using XPS measurements of this blend cast on poly(3,4-ethylenedioxythiophene):poly(styrenesulfonate) (PEDOT:PSS) and titaniumdioxide/ titaniumoxide bis(2,4-pentanedionate) electron transport layer (TiO₂:TOPD) film surfaces, which can be further processed to fabricate conventional and inverted PSCs. Detailed experiments procedures were introduced in experimental section. We examined the surface component information by estimating the carbon/sulfur (C/S) atomic ratio, as the S atom is the characteristic element of PffBT4T-2OD. The C/S atomic ratio can be de-convoluted from the XPS spectrum scan (Figure 3a and b) based on the peak area of C 1s at 285 eV and S 2p at 164 eV. The weight ratios of PC₇₁BM and polymer at surface can be then calculated from corresponding C/S atomic ratio, corrected using elemental sensitivity factors. Specific values are summarized in Table S1. We have observed that the surface distributions of donor and acceptor are rather similar when deposited onto different type of substrates, i.e. TiO₂ and PEDOT:PSS explored in this work (Figure 3c).²³ Both VA- and TA-treated films showed a polymer-rich top-layer with a polymer content around 80%, however, the MA-treated films contains more PC₇₁BM (between 60-70%) at the film surface, which indicated that methanol rinsing effectively drives the migration of PC₇₁BM particles towards the film surface, consistent with previous reports.²⁴ Combined with the observations from bulk morphology studies in the earlier section, we can conclude that thermal annealing increases the crystallinity of PffBT4T-2OD and domain size of PC₇₁BM clusters without any observable impact on vertical component redistribution. Methanol rinsing therefore encourages the migration of PC₇₁BM towards the mixed polymer-rich phase as well as towards the film surface on both substrates.

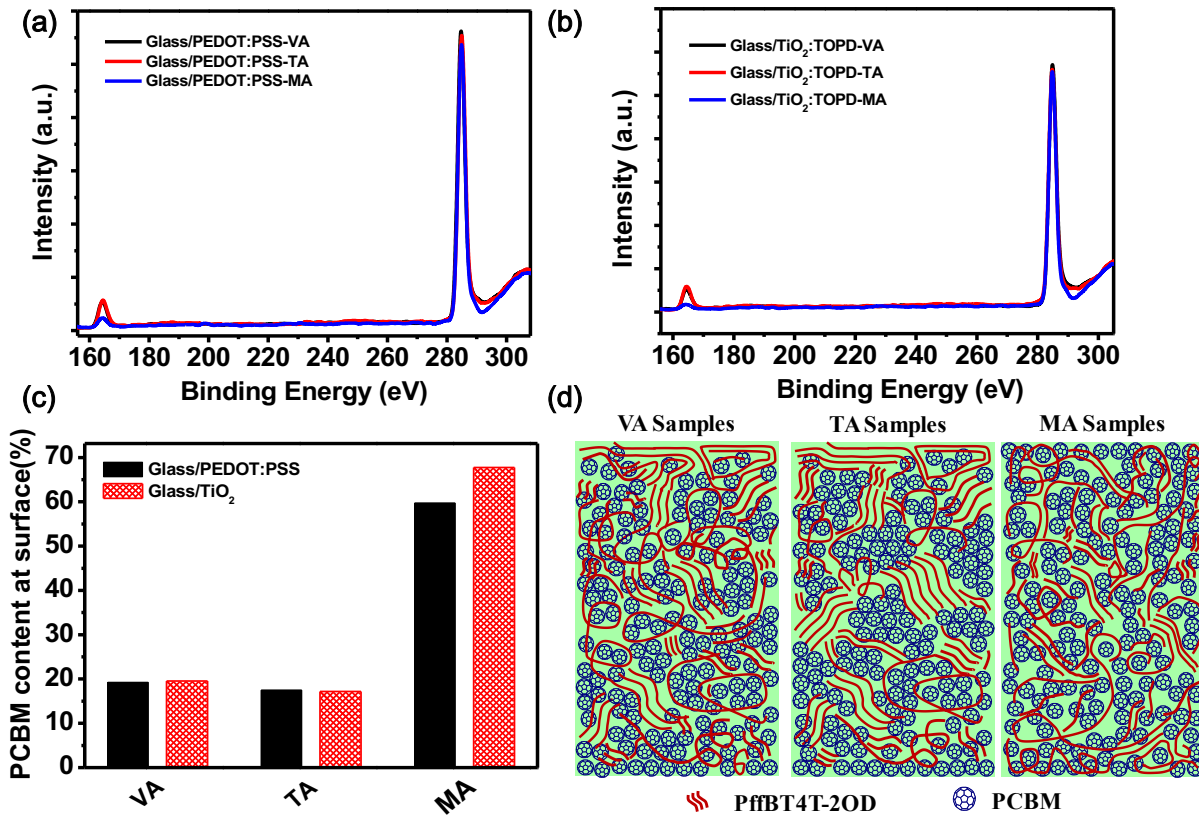


Figure 3. XPS spectra of PffBT4T-2OD:PC₇₁BM blend films after different post-treatments cast on (a) PEDOT:PSS and (b) TiO₂:TOPD surfaces. (c) Plots of PCBM content at the PffBT4T-2OD:PC₇₁BM film surface. (d) Schematic of the nanoscale morphology in VA-, TA- and MA-treated PffBT4T-2OD:PC₇₁BM blend films.

Table 2. Surface free energy of PffBT4T-2OD:PC₇₁BM blend films after different post-treatments cast on PEDOT:PSS and TiO₂ substrates.

Substrate	Treatments	Surface free energy (mJ m ⁻²)
PEDOT:PSS	VA	20.3
	TA	20.0
	MA	22.0
TiO ₂ :TOPD	VA	20.0
	TA	20.1
	MA	23.5

Further, surface free energy of the PffBT4T-2OD:PC₇₁BM blend upon different treatments was obtained based on the water contact angle (WCA) measurements to provide more intuitive

information on the surface components of the blend film (Table 2). Neat PffBT4T-2OD film has a relatively low surface free energy of *ca.* 18.5 mJ m⁻², in contrast to a much higher surface free energy of *ca.* 35.5 mJ m⁻² of PC₇₁BM. VA and TA treated blend films cast on either PEDOT:PSS or TiO₂ substrate exhibited similar surface free energy *ca.* 20.0 mJ m⁻², suggesting that the material locating at the film surface is primarily PffBT4T-2OD. However, the surface free energy of the blend cast on PEDOT:PSS and TiO₂ increased to 22.0 and 23.5 mJ m⁻² respectively after MA treatment, indicating that more PCBM has migrated to the film surface to increase the free energy. Our surface free energy analysis therefore agrees with and confirms the validity of our XPS measurements.

Intuitively, the contrasting vertical component distributions will link either unfavorably or favorably with interfacial contacts, and thus impact differently on device performance in conventional and inverted configuration.²⁴⁻²⁶ More specifically, a PC₇₁BM-rich layer near the PSC cathode and a polymer-rich layer near the PSC anode would facilitate charge transport and reduce charge recombination, and subsequently enhance device PCE.^{24,27,28} To confirm this, we have fabricated six kinds of devices receiving three post-treatments in both conventional and inverted configurations. The J-V characteristics of these devices are shown in Figure 4 and detailed photovoltaic parameters are summarized in Table 3. In a conventional configuration, the VA-treated device exhibits a relatively low PCE with a Voc of 0.715 V and a FF of 64.6%. The performance can be improved by TA- and MA-treatments with enhancements in both Voc and FF, although the Jscs of these devices are slightly decreased. As there are no significant changes over the light absorption of these films (see Figure S1), a lower Jsc is likely due to reduced charge generation and collection. Among these features, the biggest change would be the increase of FF from around 65% in VA- and TA-treated devices to 72.7% for the MA-treated device. The redistribution of the PC₇₁BM component in the film surface to form a PC₇₁BM-rich surface layer, i.e. in contact with cathode of the conventional device, will contribute to this, as it favors electron transport towards the cathode and reduces charge

recombination at this interface. This brings a notable increase in device PCE to 10.3%, more efficient than TA treatment although it increases the molecular order in the BHJ layer. In the VA- and TA-treated devices, however, the surface layer near the cathode interface is polymer-rich, therefore charge recombination is more prominent so the device FF is low.

In an inverted configuration, the surface enrichments of PffBT4T-2OD near the top interfaces in VA- and TA-treated devices would favor hole transport toward the anode, and the surface enrichments of PC₇₁BM near anode would obstruct hole transport and induce more charge recombination in principle. However, a FF of around 75% was obtained in all these devices, and PCEs of 10.7% were obtained in both VA- and MA-treated devices. The PCE of the TA-treated device received a slightly lower PCE of 10.2%, mainly due to a reduced Jsc. Vertical component distribution therefore does not correlate with device performance in inverted PffBT4T-2OD:PC₇₁BM. To shed light on these observations, we have conducted further electrical characteristic tests on those devices.

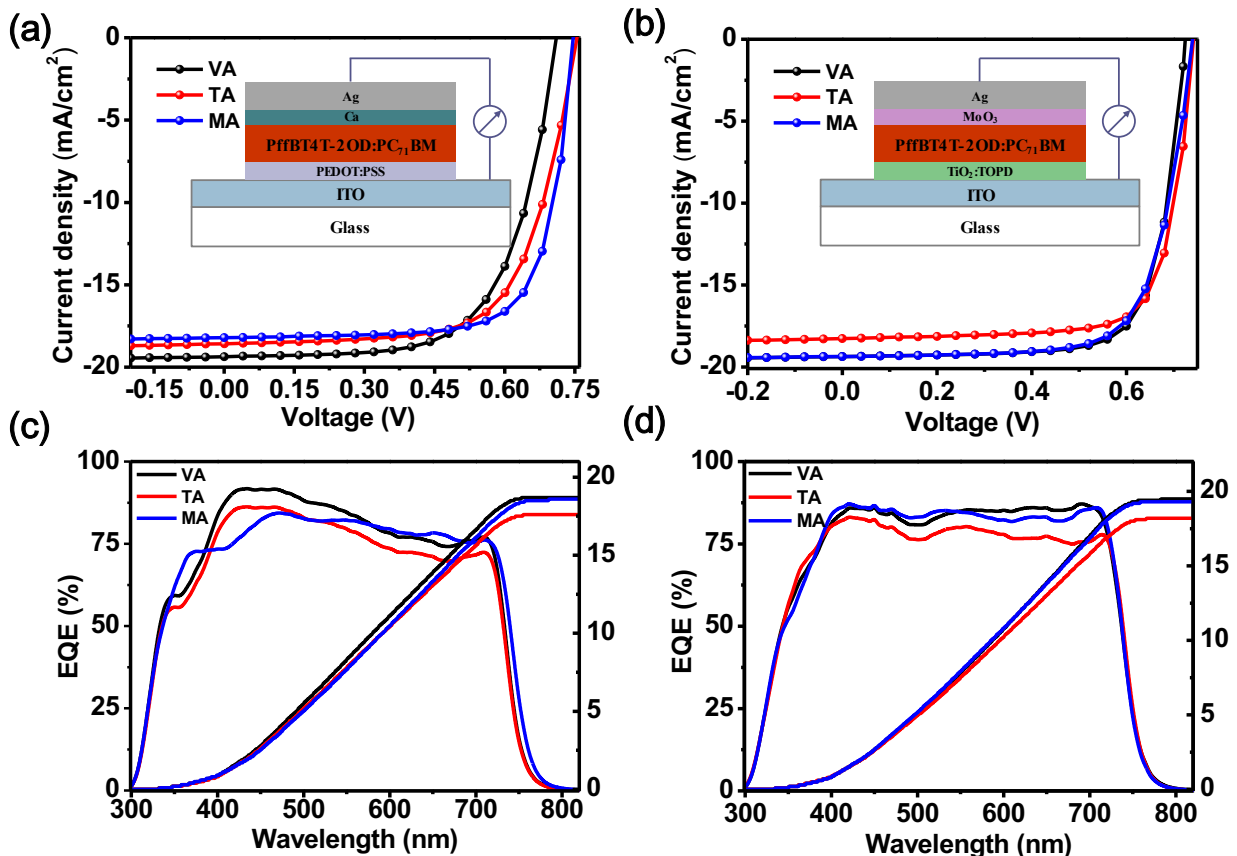


Figure 4. (a and b) Champion J-V curves, and (c and d) EQE spectra of (a, c) conventional and (b, d) inverted PSCs with different post-treatments.

Table 3. Device metrics of PffBT4T-2OD:PC₇₁BM PSCs. The average PCEs were obtained based on 32 individual devices

Device Structure	Treatments	PCE _{max} (PCE _{ave}) (%)	FF (%)	J _{sc} (mA/cm ²)	V _{oc} (V)	R _s (Ω cm ²)	R _{sh} (Ω cm ²)
Direct	VA	9.0 (8.6±0.3)	64.6	19.45	0.715	7.4	379.5
	TA	9.3 (9.1±0.2)	66.6	18.58	0.753	8.1	478.4
	MA	10.3 (9.6±0.3)	72.7	18.90	0.746	6.7	452.5
Inverted	VA	10.7 (10.4±0.2)	75.7	19.26	0.733	3.5	460.3
	TA	10.2 (9.7±0.1)	75.0	18.27	0.741	3.9	429.6
	MA	10.7 (10.4±0.2)	74.6	19.54	0.736	3.6	516.9

To explore the charge recombination mechanism, we investigated the V_{oc} vs. light intensity characteristics in both conventional and inverted devices as shown in Figure 5a and d, respectively. The V_{oc} can scale almost linearly with the light intensity in a semi-logarithmic plot. The slope of the fitted line relates to nkT/q , where n is defined as the ideality factor of the device, k is the Boltzmann constant and q is elementary charge.^{29,30} A slope greater than one suggested the increase in bimolecular charge recombination. The slopes of VA- and TA-treated conventional devices exhibited relatively high slopes of $1.72 kT/q$ and $1.50 kT/q$, which indicate serious bimolecular charge recombination in these devices. This increased charge recombination can be ascribed to the blocking effect on electron transfer of the polymer-rich top layer near the cathode. The MA-treated device recorded the lowest slope of $1.28 kT/q$, indicating the least extent of bimolecular recombination. For all the inverted devices the slopes are close to $1.20 kT/q$, which indicated efficient charge transport. As summarized in Table 3, all inverted devices exhibited a high FF close to 75%, a characteristic that is consistent with the charge recombination investigation here.

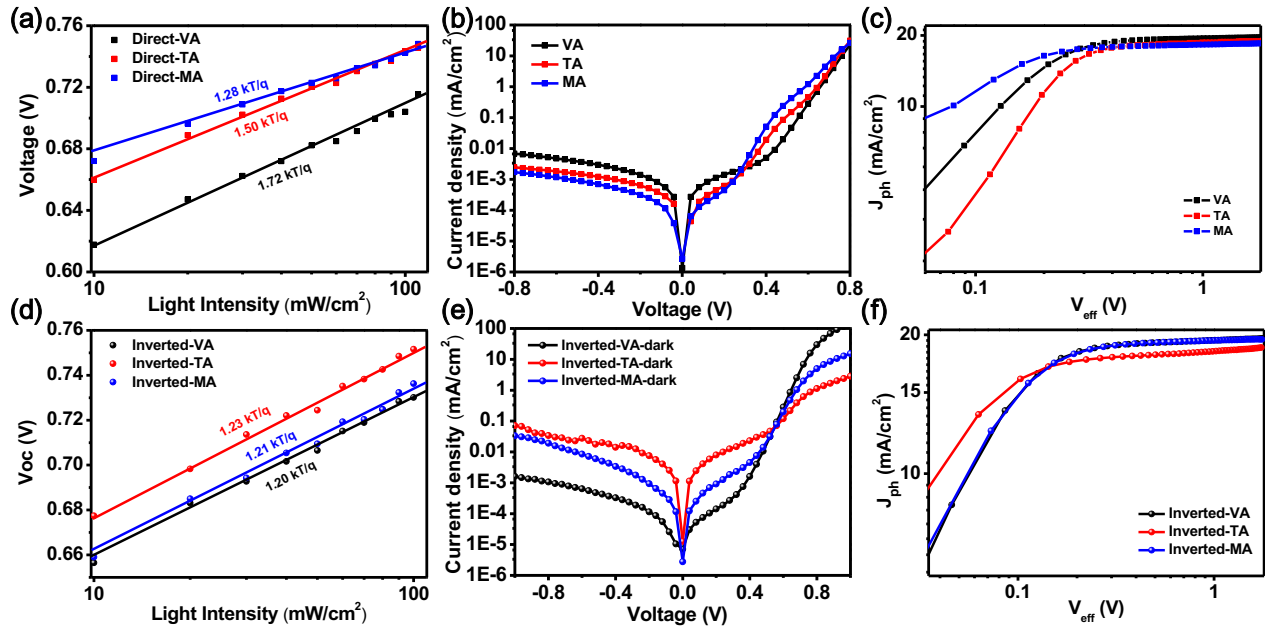


Figure 5. Light-intensity dependent open-circuit voltages of (a) conventional and (d) inverted devices. Dark J-V curves for (b) conventional and (e) inverted devices. And photocurrent density (J_{ph}) versus effective voltage curves (V_{eff}) of (c) conventional and (f) inverted devices.

Dark J-V curves were plotted in Figure 5b and e to examine the device rectification properties, which are strongly related with charge blocking properties. The MA-treated device exhibited the highest rectification ratio in the conventional configuration, with the smallest current leakage density, which indicates a better contact between the photoactive layer and cathode. However, the situation is reversed for the VA-treated devices. The inverted VA-treated devices exhibited the smallest leakage current density under reverse voltage and the highest forward current under forward voltage. The MA-treated devices have moderate rectification properties, which indicate that charge transport would be less influenced by the unfavorable vertical component distributions. The TA-treated devices showed worse rectification properties, with the highest leakage current density. Exciton dissociation efficiency and recombination properties can be determined from J-V curves under illumination and dark conditions to investigate the relationship between J_{ph} and V_{eff} , with J_{ph} was defined as the difference between current density under illumination (J_L) and current density in the dark (J_D), and V_{eff} was defined as $V_0 - V$ where V_0 is the voltage when $J_{ph} = 0$ and V is applied bias voltage.³¹ It is seen that the

photocurrent increased linearly with voltage at low V_{eff} , and then saturated at high V_{eff} where most of the e-h pairs were completely dissociated and driven to electrode. The charge collection probability (P_c) can be defined as $J_{\text{ph}}/J_{\text{ph,sat}}$, and can be applied to examine the charge block and collection behavior. Charge collection probability (P_c) of VA-, TA- and MA-treated devices in a conventional configuration are 97.8%、97.9% and 99.0%, respectively. However, the collection behavior in all inverted devices is very efficient, with all devices having a P_c exceeding 99% although that of the TA-treated devices is slightly lower. Figure S2 shows the Nyquist plots of impedance spectra measurements for conventional and inverted devices, respectively. The data were fitted with a double RC in parallel connection equivalent circuit modeling. Interestingly, the interface resistance (R_s) varied sharply from 118, 123 to 61 Ω for VA-, TA- and MA-treated conventional devices respectively. However, R_s changed to a much lesser extent, with values of 43, 65 and 54 Ω for VA-, TA- and MA-treated inverted devices. These optoelectronic characterization results again support our previous conclusion from J-V measurements that these post-treatments have less influence on device performance in an inverted configuration.

Finally, we evaluate the different charge block behavior in these devices using hole-only devices with a configuration of glass/ITO/PEDOT:PSS/Active layer/MoO₃/Ag. For VA- and TA- treated devices, the current-voltage curves under dark conditions showed distinctly asymmetric J-V curves (see Figure 6a), so that the variations of vertical component distribution should bring notable changes to device performance, with a polymer-rich region near cathode will seriously hampers electron injection to the cathode (see Figure 6b), as our device results have supported. However, the current density-voltage curve is symmetric for the MA-treated device, which indicates that holes can be effectively injected from either side of both conventional and inverted devices, that is to say, around 65% of polymer donor near the surface region (see our XPS results) does little to inhibit vertical charge transport (see scheme in Figure 3d). This observation is not unusual, with previous works

having reported similar results; devices with 75 % of P3HT at the air surface were also found to have a negligible impact on device performance.³²

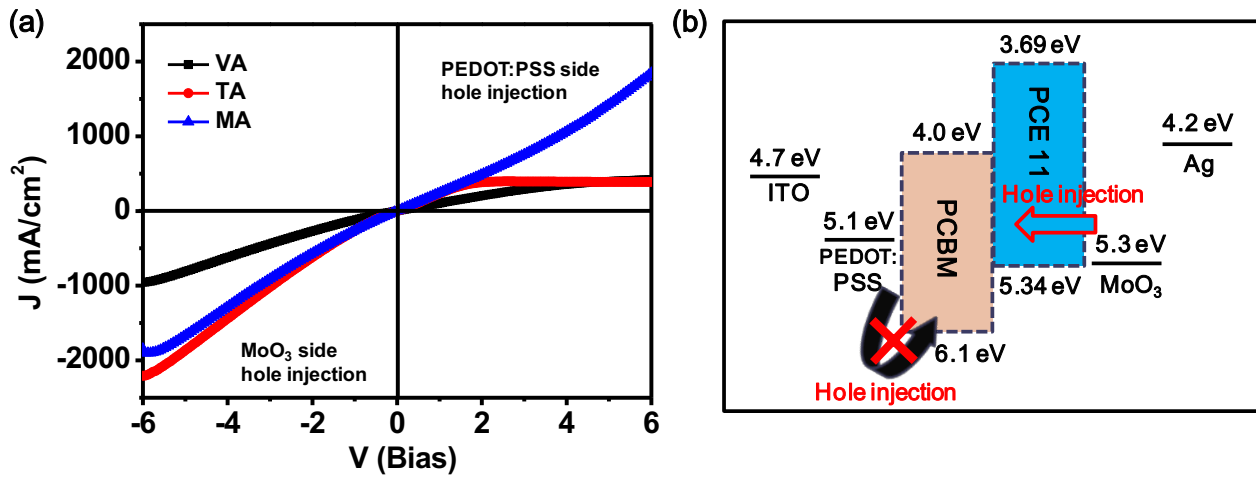


Figure 6. (a) The linear J-V curves of the hole-only devices prepared in different DIO extraction procedures. (b) Corresponding energy level diagram for the injection of holes for the hole-only device.

4. CONCLUSION

We have investigated the nanoscale morphology changes of PffBT4T-2OD:PC₇₁BM solar cells in both lateral and vertical directions upon vacuum, thermal annealing and methanol rinsing post-treatments. We found that thermal annealing increased the crystallinity of PffBT4T-2OD and the domain size of PC₇₁BM clusters, whilst methanol rinsing reduces the crystallinity of PffBT4T-2OD and facilitates the diffusion of PC₇₁BM into the mixed PffBT4T-2OD:PC₇₁BM phase as well as towards the film surface, on both PEDOT:PSS and TiO₂ composite surfaces. The polymer-rich surface region in vacuum- and thermal annealing- treated conventional devices obstructs electron injection towards the cathode, and reduces the maximum achievable device efficiency, while conversely this polymer-rich surface region is beneficial in the inverted devices. However, although a PC₇₁BM-rich region will locate at the cathode or anode interface upon methanol rinsing treatment in conventional and inverted devices respectively, holes can be effectively injected from both sides of the device to

ensure effective charge transport, as supported by a number of optoelectronic property investigations. The influences of vertical component distribution therefore cannot be summarized in a simple conclusion, and complex results may be obtained depending on the device configuration.

ASSOCIATED CONTENT

Supporting Information. The following files are available free of charge: C, S contents at surface extracted from XPS spectra; UV-Vis spectra of PffBT4T-2OD:PC₇₁BM and Nyquist plots of impedance spectra of direct and inverted configurations.

AUTHOR INFORMATION

Corresponding Author

* E-mail: twang@whut.edu.cn

Author Contributions

The manuscript was written through contributions of all authors. All authors have given approval to the final version of the manuscript.

ACKNOWLEDGMENT

The work is supported by the National Natural Science Foundation of China (Grant No. 21774097, 21504065), and the Natural Science Foundation of Hubei Province (Grants No. 2018CFA055). TW also acknowledges support from the Recruitment Program of Global Experts (1000 Talents Plan) of China. The authors thank the Engineering and Physical Sciences Research Council for support. We thank beamline BL16B1 at Shanghai Synchrotron Radiation Facility (China) for providing beam time and help during our GISAXS experiments, and thank Dr. Zhihong Chen (Department of Physics, Wuhan University of Technology) for helping with the GISAXS data analysis. We also thank

Diamond Light Source for access to beamline I07 (SI17223-1) that contributed to the GIWAXS results.

REFERENCES

- (1) Zhao, L.; Zhao, S.; Xu, Z.; Yang, Q.; Huang, D.; Xu, X. A Simple Method to Adjust the Morphology of Gradient Three-Dimensional PTB7-Th:PC₇₁BM Polymer Solar Cells. *Nanoscale* **2015**, *7* (12), 5537-5544.
- (2) Zhong, H.; Li, C.; Carpenter, J.; Ade, H.; Jen, A. Influence of Regio- and Chemoselectivity on the Properties of Fluoro-Substituted Thienothiophene and Benzodithiophene Copolymers. *J. Am. Chem. Soc.* **2015**, *137* (24), 7616-7619.
- (3) He, Z.; Zhong, C.; Su, S.; Xu, M.; Wu, H.; Cao, Y. Enhanced Power-Conversion Efficiency in Polymer Solar Cells Using an Inverted Device Structure. *Nat. Photon.* **2012**, *6* (9), 591-595.
- (4) Cui, Y.; Yao, H.; Yang, C.; Zhang, S.; Hou, J.; Organic Solar Cells with an Efficiency Approaching 15%. *Acta Polym. Sin.* **2018**, No. 2, 223-230.
- (5) Xiao, Z.; Jia, X.; Ding, L. Ternary Organic Solar Cells Offer 14% Power Conversion Efficiency. *Sci. Bull.* **2017**, *62* (23), 1562-1564.
- (6) Hoppe, H.; Sariciftci, N. Organic Solar Cells: An Overview. *J. Mater. Research* **2004**, *19* (7), 1924-1945.
- (7) Lu, L.; Zheng, T.; Wu, Q.; Schneider, A.; Zhao, D.; Yu, L. Recent Advances in Bulk Heterojunction Polymer Solar Cells. *Chem. Rev.* **2015**, *115* (23), 12666-12731.
- (8) Heeger, A. 25th Anniversary Article: Bulk Heterojunction Solar Cells: Understanding the Mechanism of Operation. *Adv. Mater.* **2014**, *26* (1), 10-28.
- (9) Liu, Y.; Zhao, J.; Li, Z.; Mu, C.; Ma, W.; Hu, H.; Jiang, K.; Lin, H.; Ade, H.; Yan, H. Aggregation and Morphology Control Enables Multiple Cases of High-Efficiency Polymer Solar Cells. *Nat. Commun.* **2014**, *5*, 5293.

- (10) Zhao, J.; Li, Y.; Yang, G.; Jiang, K.; Lin, H.; Ade, H.; Ma, W.; Yan, H.; Efficient Organic Solar Cells Processed from Hydrocarbon Solvents. *Nat. Energy*, **2016**, *1* (2), 15027.
- (11) Li, N.; Perea, J.; Kassar, T.; Richer, M.; Heumueller, T.; Matt, G.; Hou, Y.; Güldal, N.; Chen, H.; Chen, S.; Langner, S.; Berlinghof, M.; Unruh, T.; Brabec, C. Abnormal Strong Burn-in Degradation of Highly Efficient Polymer Solar Cells Caused by Spinodal Donor-Acceptor Demixing. *Nat. Commun.* **2017**, *8*, 14541.
- (12) Pearson, A.; Hopkinson, P.; Couderc, E.; Domanski, K.; Abdi-Jalebi, M.; Greenham, N. Critical Light Instability in CB/DIO Processed PBDTTT-EFT:PC₇₁BM Organic Photovoltaic Devices. *Org. Electron.* **2016**, *30*, 225-236.
- (13) Tremolet de Villers, B.; Hara, K.; Ostrowski, D.; Biddle, P.; Shaheen, S.; Chabinye, M.; Olson, D.; Kopidakis, N. Removal of Residual Diiodooctane Improves Photostability of High Performance Organic Solar Cell Polymers. *Chem. Mater.* **2016**, *28* (3), 876-884.
- (14) Yan, Y.; Cai, F.; Yang, L.; Li, J.; Zhang, Y.; Qin, F.; Xiong, C.; Zhou, Y.; Lidzey, D.; Wang, T. Light-Soaking-Free Inverted Polymer Solar Cells with an Efficiency of 10.5% by Compositional and Surface Modifications to a Low-Temperature-Processed TiO₂ Electron-Transport Layer. *Adv. Mater.* **2017**, *29* (1), 1604044.
- (15) Zhang, Y.; Parnell, A.; Pontecchiani, F.; Cooper, J.; Thompson, R.; Jones, R.; King, S.; Lidzey, D.; Bernardo, G. Understanding and Controlling Morphology Evolution via DIO Plasticization in PffBT4T-2OD/PC₇₁BM Devices. *Sci. Rep.* **2017**, *7*, 44269.
- (16) Wang, T.; Pearson, A.; Lidzey, D.; Jones, R. Evolution of Structure, Optoelectronic Properties, and Device Performance of Polythiophene:Fullerene Solar Cells During Thermal Annealing. *Adv. Funct. Mater.* **2011**, *21*, 1383-1390.

- (17) Wang, T.; Scarratt, N.; Yi, H.; Coleman, I.; Zhang, Y.; Grant, R.; Yao, J.; Skoda, M.; Dunbar, A.; Jones, R.; Iraqi, A.; Lidzey, D. Vertical Stratification and Its Impact on Device Performance in a Polycarbazole Based Copolymer Solar Cells. *J. Mater. Chem. C* **2015**, *3* (16), 4007-4015.
- (18) Wang, T.; Pearson, A.; Lidzey, D. Correlating Molecular Morphology with Optoelectronic Function in Solar Cells Based on Low Band-gap Copolymer:fullerene Blends. *J. Mater. Chem. C* **2013**, *1* (44), 7266-7293.
- (19) Ma, W.; Yang, G.; Jiang, K.; Carpenter, J.; Wu, Y.; Meng, X.; McAfee, T.; Zhao, J.; Zhu, C.; Wang, C.; Ade, H.; Yan, H. Influence of Processing Parameters and Molecular Weight on the Morphology and Properties of High-Performance PffBT4T-2OD:PC₇₁BM Organic Solar Cells. *Adv. Energy Mater.* **2015**, *5* (23), 1501400.
- (20) Liao, H., Tsao, C., Lin, T.; Chuang, C.; Chen, C.; Jeng, U.; Su, C.; Chen, Y.; Su, W. Quantitative Nanoorganized Structural Evolution for a High Efficiency Bulk Heterojunction Polymer Solar Cell. *J. Am. Chem. Soc.* **2011**, *133* (33), 13064.
- (21) Li, W.; Cai, J.; Cai, F.; Yan, Y.; Yi, H.; Gurney, R.; Liu, D.; Iraqi, A.; Wang, T. Achieving over 11% Power Conversion Efficiency in PffBT4T-2OD-based Ternary Polymer Solar Cells with Enhanced Open-Circuit-Voltage and Suppressed Charge Recombination. *Nano Energy* **2018**, *44*, 155.
- (22) Li, W.; Yan, Y.; Gong, Y.; Cai, J.; Cai, F.; Gurney, R.; Liu, D.; Pearson, A.; Lidzey, D.; Wang, T. Contrasting Effects of Energy Transfer in Determining Efficiency Improvements in Ternary Polymer Solar Cells. *Adv. Funct. Mater.* **2018**, *28* (5), 1704212.
- (23) Yan, Y.; Liu, X.; Wang, T. Conjugated-Polymer Blends for Organic Photovoltaics: Rational Control of Vertical Stratification for High Performance. *Adv. Mater.* **2017**, *20*, 1601674.
- (24) Xiao, Z.; Yuan, Y.; Yang, B.; VanDerslice, J.; Chen, J.; Dyck, O.; Duscher, G.; Huang, J. Universal Formation of Compositionally Graded Bulk Heterojunction for Efficiency Enhancement in Organic Photovoltaics. *Adv. Mater.* **2014**, *26* (19), 3068-3075.

- (25) Guerrero, A.; Dörling, B.; Ripolles-Sanchis, T.; Aghamohammadi, M.; Barrena, E.; Campoy-Quiles, M.; Garcia-Belmonte, G. Interplay between Fullerene Surface Coverage and Contact Selectivity of Cathode Interfaces in Organic Solar Cells. *ACS Nano*, **2013**, *7* (5), 4637-4646.
- (26) Ye, L.; Jing, Y.; Guo, X.; Sun, H.; Zhang, S.; Zhang, M.; Huo, L.; Hou, J. Remove the Residual Additives toward Enhanced Efficiency with Higher Reproducibility in Polymer Solar Cells. *J. Phys. Chem. C* **2013**, *117* (29), 14920-14928.
- (27) Sun, Q.; Zhang, F.; Wang, J.; An, Q.; Zhao, C.; Li, L.; Teng, F.; Hu, B. A Two-Step Strategy to Clarify the Roles of a Solution Processed PFN Interfacial Layer in Highly Efficient Polymer Solar Cells. *J. Mater. Chem. A* **2015**, *3* (36), 18432-18441.
- (28) Sun, Q.; Zhang, F.; Wang, J.; An, Q.; Zhang, M.; Wang, J.; Zhang, J. Highly Efficient Polymer Solar Cells by Step-by-Step Optimizing Donor Molecular Packing and Acceptor Redistribution. *Phys. Chem. Chem. Phys.* **2017**, *19* (1), 709-716.
- (29) Nalwa, K.; Mahadevapuram, R.; Chaudhary, S. Growth Rate Dependent Trap Density in Polythiophene-Fullerene Solar Cells and Its Implications. *Appl. Phys. Lett.* **2011**, *98* (9), 093306.
- (30) Koster, L.; Mihailetschi, V.; Ramaker, R.; Blom, P. Light Intensity Dependence of Open-Circuit Voltage of Polymer:Fullerene Solar Cells. *Appl. Phys. Lett.* **2005**, *86* (12), 123509.
- (31) Xie, Y.; Zhou, W.; Yin, J.; Hua, X.; Zhang, L.; Meng, X.; Ai, Q.; Chen, Y. Post-Annealing to Recover the Reduced Open-Circuit Voltage Caused by Solvent Annealing in Organic Solar Cells. *J. Mater. Chem. A* **2016**, *4* (16), 6158-6166.
- (32) Germack, D.; Chan, C.; Kline, R.; Fischer, D.; Gundlach, D.; Toney, M.; Richter, L.; DeLongchamp, D. Interfacial Segregation in Polymer/Fullerene Blend Films for Photovoltaic Devices. *Macromolecules* **2010**, *43* (8), 3828-3836.

Table of Contents Entry

The nanoscale morphology changes in both lateral and vertical directions in PffBT4T-2OD:PC₇₁BM solar cells are investigated and correlated with device performance having either conventional or inverted configuration.

